ELSEVIER

Journal of Fluids and Structures 19 (2004) 835–850

JOURNAL OF FLUIDS AND STRUCTURES

www.elsevier.nl/locate/jnlabr/yjfls

Evaluation of a fictitious domain method for predicting dynamic response of mechanical heart valves

J.M.A. Stijnen[a,*], J. de Hart[b], P.H.M. Bovendeerd[a], F.N. van de Vosse[a]

[a] *Department of Biomedical Engineering, Eindhoven University of Technology, P.O. Box 513, MB Eindhoven 5600, The Netherlands*
[b] *Division of Cardio-thoracic Surgery, Academic Medical Center, University of Amsterdam, Building W-Hoog, Room 4.117, P.O. Box 22700, DE Amsterdam 1100, The Netherlands*

Received 24 July 2003; accepted 16 April 2004

Abstract

Flow phenomena around heart valves are important for the motion of the valve leaflets, hence the dynamics of the valve. This work presents an evaluation of a two-dimensional moving rigid heart valve, in which a fictitious domain method is used to describe fluid–structure interaction. Valve motion and fluid flow around the valve were computed for several Reynolds and Strouhal numbers. Particle Image Velocimetry measurements in an in vitro experimental set-up were performed to validate the computational results. The influences of variations of the flow-pulse, expressed in Reynolds and Strouhal number, are well predicted by the computational method. As the fictitious domain method can readily be applied to fully three-dimensional fluid–structure interaction problems, this study indicates that this method is well suited for the analysis of valve dynamics and ventricular flow in physiologically realistic geometries.

1. Introduction

The four valves of the heart maintain the unidirectional flow of blood through the heart. Pathologies of one or more of the valves may cause significant limitation of their function and subsequently the pump function of the heart. The diseased valve may not be able to fully close, causing leakage (regurgitation), or it may not be able to open properly (stenosis), obstructing the blood to enter or leave the heart. The function of one of the valves may be compromised to an extent that valve replacement is desired. In many cases a mechanical prosthesis will be chosen, because of its high durability. Several different shapes of valve prostheses have been developed and evaluated in the past (Chandran et al., 1989).

Compared to the natural valve, these prostheses have several drawbacks in common with respect to their haemodynamic performance, like increased transvalvular pressure gradient, increased backflow during closure and increased shear stresses in the blood causing damage to or activation of blood platelets (Chandran et al., 1989). These phenomena are all related to the design and properties of the valve.

In-vivo, in-vitro and numerical studies are commonly used to investigate the relation between valve design and function. In-vivo investigation of flow through heart valves is possible, for example using ultrasound (Pop et al., 1989) or MR-techniques (Walker et al., 1996; Kilner et al., 2000). While in-vivo studies assess valve function in the final application, in-vitro set-ups allow for a more controllable, accessible and reproducible assessment the behaviour of prosthetic valves. In such set-ups several techniques have been used such as flow visualization (Reul et al., 1981;

*Corresponding author. Tel.: +31-40-2474837; fax: +31-40-2447355.
E-mail address: j.m.a.stignen@tue.nl (J.M.A. Stijnen).

0889-9746/$ - see front matter
doi:10.1016/j.jfluidstructs.2004.04.007

Chandran et al., 1989; Lim et al., 2001), pressure drop measurements (Chandran et al., 1989; Pop et al., 1989; Garitey et al., 1995; Cape et al., 1996), regurgitant flow measurements (Chandran et al., 1989), velocity measurements using ultrasound (Pop et al., 1989; Garitey et al., 1995), LDA (Fatemi and Chandran, 1989; King et al., 1996; Grigioni et al., 2001) and DPIV (Bluestein et al., 2000; Lim et al., 2001; Vlachos et al., 2001). Experimental studies also have some drawbacks: they are expensive, labour intensive and not flexible with respect to geometrical variations.

Computational Fluid Dynamics (CFD) models are more flexible in applying variations in geometry, and less expensive in constructing. Thus, CFD models are a useful tool to reduce the amount of experiments necessary. Moreover, they can provide information that is hard, or even impossible, to measure.

In some CFD models, flow around heart valves in fixed position is studied (King et al., 1996; Krafczyk et al., 1998; Lemmon and Yoganathan, 2000; Bluestein et al., 2002). These models are suitable for analysing transvalvular pressure drop and shear stresses at the surface of the valve leaflets. In order to study the pump function of the heart, however, analysis of valve motion is necessary.

The behaviour of an opening and closing valve depends on the interaction between the motion of the valve and the motion of the surrounding fluid. Furthermore, when investigating the pump function of the left heart, i.e. ejection fraction, it has to be noted that there is an interaction between the mitral and aortic valve: the opening timing of one valve is influenced by the closing behaviour of the other valve. Hence, in order to study the dynamics of a mechanical valve prosthesis and the associated pump function of the ventricle, valve motion and time-dependent fluid–structure interaction has to be taken into account in the computational model.

Also, computational models of moving valves have been published in the last three decades (Peskin, 1972; Peskin and McQueen, 1995; Horsten, 1990; de Hart et al., 2000, 2003; Baccani et al., 2003). Baccani et al. (2003) prescribed the velocity of a moving valve as a boundary condition on the fluid. In this way, no real interaction between valve and fluid motion was taken into account and it was not necessary to adapt the computational grid of the fluid domain to the position of the valve.

In order to allow the local coupling of fluid and valve properties, the mesh of the fluid domain will have to be updated to follow the motion of the valve. One way to do this is the use of an Arbitrary Lagrange–Eulerian (ALE) method with a moving grid for the velocity domain. This method was used by Horsten (1990) for modelling a moving aortic valve leaflet in a pulsatile flow, and by Vierendeels et al. (2000) for the analysis of the filling of a deforming axisymmetric ventricle, where no valve was present in the mitral orifice. In this method, the positions of the computational grid of the fluid are adapted based on the position of the moving valve (Horsten, 1990) or moving ventricle wall (Vierendeels et al., 2000), while maintaining the grid topology. When analysing flow through moving valves, the large translations of the valve leaflets cause the quality of the grid to degenerate rapidly. Complete closure of an initially opened valve is not possible using this method.

In order to maintain the quality of the computational grid, remeshing combined with an ALE-technique can be applied. This method is more commonly used in solid mechanics (Kwak and Im, 2003). Remeshing requires interpolation techniques to transfer state variables from the old mesh to the new one, which may introduce additional inaccuracies. Furthermore, remeshing is a computationally expensive technique and may be very difficult to apply for three-dimensional problems.

One of the most advanced models incorporating fluid–structure interaction is a left ventricle model by Peskin (Peskin, 1972; Peskin and McQueen, 1995). In this model the immersed boundary technique is used, which effectively uses local volume forces on the fluid to account for the interaction between the fluid and the heart wall and the valves. In this way there is no need to change the fluid mesh, thus avoiding the corresponding problems described above. However, to guarantee the stability of the numerical technique used, the viscosity was increased to 25 times that of blood, resulting in a Reynolds number in the order of magnitude of 80, which is 25 times lower than physiological (Peskin and McQueen, 1995). Lemmon and Yoganathan (2000) used Peskin's immersed boundary technique and applied a semi-implicit method for pressure-linked equations (Patankar, 1983) to provide solution stability for physiological Reynolds numbers. However, their model did not incorporate moving heart valves.

Recently, fictitious domain methods (Glowinski et al., 1994; Bertrand et al., 1997; de Hart et al., 2000; Baaijens, 2001) have been introduced to couple quantities on separate meshes. The method enables the coupling of velocities of a structure to fluid velocities, while the structural mesh arbitrarily moves through the fluid mesh. de Hart et al. (2000) applied and validated a fictitious domain method in a two-dimensional model of a flexible aortic valve, and extended it to a three-dimensional realistic geometry (de Hart et al., 2003), for a single set of the characteristic fluid flow parameters, i.e. the Reynolds and Strouhal numbers. Successful simulation of a fluid–structure interaction problem with a very stiff elastic solid in a fluid is not trivial. The eigenvalues of the system are related to the viscosity of the fluid and to the stiffness of the solid. Since the stiffness of a mechanical valve is considerably higher than that of a flexible leaflet, the range of eigenvalues of the system to be solved is increased, which adversely affects its stability.

The objective of this work is to investigate the applicability of a fictitious domain method for simulating the motion of a stiff prosthetic heart valve leaflet. To this end, model predictions on flow fields and on timing of valve motion are compared to experimental results obtained in a quasi-two-dimensional experiment. To evaluate the sensitivity of the computational method to variations in the characteristic fluid flow parameters, expressed in the Reynolds and Strouhal numbers, a range of flow-pulses was used in the computational method and the results were compared to the respective experimental findings.

2. Methods

2.1. Experimental method

To validate the predictions of the two-dimensional version of the computational model an experimental set-up, based on the one used by de Hart et al. (2000), was used. The geometry of the measurement section, shown in Fig. 1, is a quasi-two-dimensional representation of a cross-section of a stiff aortic valve with a sinus cavity.

It consists of a plexiglas channel with a height H of 20 mm and length $6H$. Halfway along the length of the channel is a cylindrical cavity, representing the sinus cavity of the aortic valve, with radius R equal to H. In order to obtain a two-dimensional flow field in the centre plane of the channel, the width of the channel is $6H$. At the upstream side of the sinus cavity a stiff strip of lexane is fixed to the top of the channel. The fixation was realised using three pieces of water-resistant adhesive tape, one next to the centre of the channel and two near the side walls. The width of the adhesive tape was 5 mm, in order to keep the bending stiffness low. The measurement section was mounted in a pulse duplicator set-up as shown in Fig. 2.

The set-up consists of a steady pump (SP), a computer-controlled piston (P), a diffuser (D), the measurement section (MS), a reservoir combined with a resistance (R1) and a reservoir (R2). The reservoir attached to the measurement section was completely filled with fluid, such that the set-up was not compliant. To be able to obtain physiologically relevant fluid flow parameters, the fluid used was a mixture of 36% by volume of glycerol in water with a viscosity of 4.3×10^{-3} [kg/m s]. The viscosity of this mixture matches the viscosity of blood assuming Newtonian constitutive behaviour.

The flow-pulse used is shown in Fig. 3. The pulsatile flow rate is obtained as follows. The steady pump creates a stationary flow rate, on top of which a pulsating flow is superimposed by applying a periodic motion of the computer-controlled piston. The forward motion of the piston results in a flow rate higher than the stationary component and lasts $0.38T$, with T the time period of the signal. The reversed stroke of the piston lasts the rest of the time period. The resulting flow-pulse resembles the physiological aortic flow-pulse, in the sense that there is a large systolic flow peak lasting approximately 38% of the cardiac cycle and a relatively low flow rate throughout the rest of the cardiac cycle. This choice enabled a variation of the Reynolds and Strouhal numbers, by variation of the amplitude and frequency of the piston motion, without changing the characteristics of the flow-pulse.

The flow is characterized by the Reynolds and Strouhal numbers, given by

$$\mathrm{Re} = \frac{\rho V H}{\eta}, \quad \mathrm{Sr} = \frac{H}{TV}, \tag{1}$$

with ρ the fluid density, V the average peak velocity over the height H of the channel, η the dynamic viscosity of the fluid, and T a time constant chosen to be the time period.

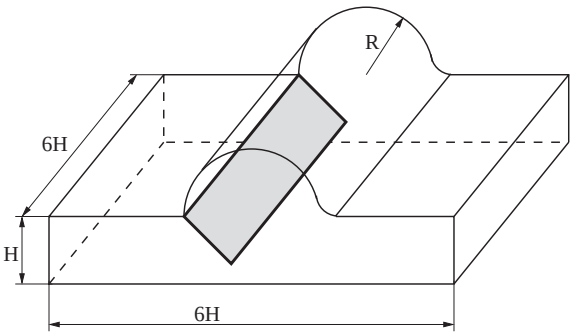

Fig. 1. Schematic drawing of the geometry of the measurement section.

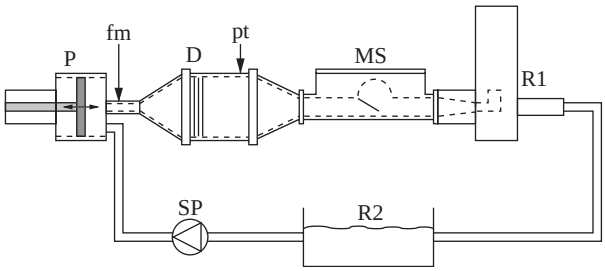

Fig. 2. Schematic representation of the pulse duplicator. (P) Piston; (D) diffuser; (MS) measurement section; (R1, R2) reservoir; (SP) steady pump; (fm) flow meter; (pt) pressure transducer.

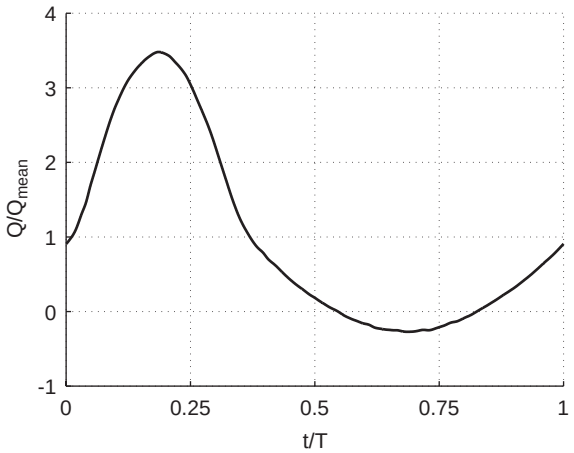

Fig. 3. Flow-pulse measured by the electromagnetic flow probe, located between the piston and the diffuser.

Table 1
Time period of the applied flow-pulse for each experiment

	Sr = 0.03	Sr = 0.055	Sr = 0.08
Re = 500	—	3.70 (case 1)	—
Re = 750	4.50 (case 2)	2.45 (case 3)	1.65 (case 4)

Several flow conditions were applied in order to study the effect on the dynamic behaviour of the valve. The amplitude of the flow-pulse was changed such that at peak flow rate the required Reynolds numbers were reached. Next, the frequency was changed in order to reach relevant Strouhal numbers. Finally, the magnitude of the steady flow component was adjusted such that the amount of backflow obtained was enough to close the valve at the end of the backflow phase. Within the possibilities of the set-up used, the Reynolds number could be varied from 500 to 750 for a Strouhal number of 0.055. For Reynolds number 750 the Strouhal number was varied both ways by 0.025. The corresponding time periods are shown in Table 1.

For each case presented in Table 1, instantaneous whole-field velocities were measured using a Particle Image Velocimetry (PIV) system (Dantec PIV-1100). To obtain the fluid velocity field using the PIV technique (Willert and Gharib, 1991; Westerweel, 1993), the fluid was seeded with light-reflecting particles (hollow glass spheres) with a mean diameter of 100 μm and a density of 1010 kg/m^3.

The seeded fluid was illuminated with a pulsed laser sheet directed through the centre plane of the measurement section. A CCD camera (Kodak ES-1.0) recorded the position of the seeding particles and the valve leaflet (see Fig. 4).

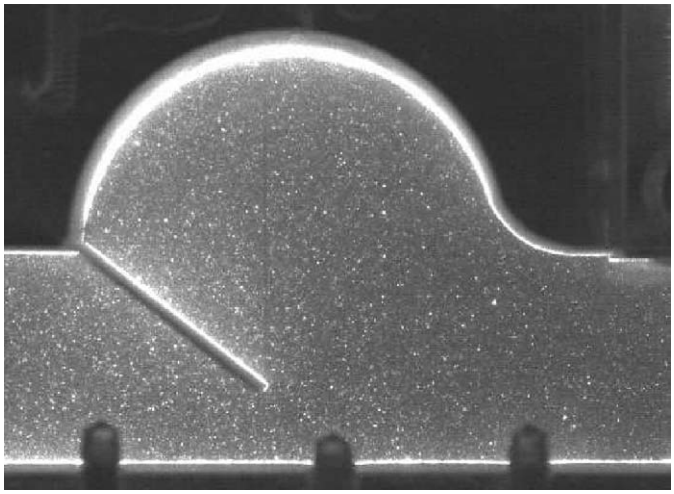

Fig. 4. Image of the PIV camera showing the sinus cavity and the stiff leaflet. Only the particles in the laser sheet are detected by the camera.

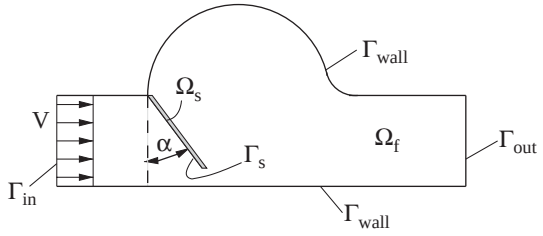

Fig. 5. Schematic representation of the geometry, the domain of the fluid (Ω_f) and solid (Ω_s) phase, the boundaries of the domains, the inflow boundary condition (V) and the definition of the opening angle of the valve (α).

The camera images of 1016 by 1008 pixels were subdivided into interrogation areas of 64×64 pixels, corresponding to 7.5×7.5 mm. A correlation technique was applied to the interrogation areas of subsequent camera images to determine the average displacement within the interrogation areas. In order to obtain good-quality correlations, the maximum particle displacement should not exceed a quarter of the interrogation area size (Willert and Gharib, 1991). To this end, the time between two subsequent images is set to 1000 μs at a maximum velocity estimated to be 0.2 m/s. A subpixel interpolation technique was used which allows for the detection of particle motion up to 0.1 times the pixel pitch. Thus, the smallest resolvable velocity would be 1.25×10^{-3} m/s. The velocity field is derived by dividing the displacement field, obtained from the correlation technique, by the time between subsequent images. The opening angle of the valve (shown in Fig. 5) is derived straightforwardly from the position shown in the camera images.

2.2. Computational method

The geometry used in the computations corresponds to the geometry of the centre plane of the experimental set-up, and is shown in Fig. 5. The fluid domain is denoted by Ω_f, the solid domain by Ω_s.

The fluid velocity is computed by solving the Navier–Stokes equation (2) and the continuity equation (3):

$$\rho\left(\frac{\partial \mathbf{v}_f}{\partial t} + \mathbf{v}_f \cdot \boldsymbol{\nabla}\mathbf{v}_f\right) = \boldsymbol{\nabla} \cdot (-p\mathbf{I} + 2\eta\mathbf{D}) + \mathbf{f}_f^* \quad \text{in} \quad \Omega_f, \tag{2}$$

$$\boldsymbol{\nabla} \cdot \mathbf{v}_f = 0 \quad \text{in} \quad \Omega_f, \tag{3}$$

where ρ represents the fluid density, $\mathbf{v}_f$ the fluid velocity field, t the time, p the pressure, η the dynamic viscosity, $\mathbf{D}$ the rate of deformation tensor $\mathbf{D} = \frac{1}{2}(\boldsymbol{\nabla}\mathbf{v}_f + (\boldsymbol{\nabla}\mathbf{v}_f)^{\mathrm{T}})$, and $\mathbf{f}_f^*$ the body forces. In the computational method, laminar flow is assumed of a Newtonian, isothermal and incompressible fluid.

At the top and the bottom of the fluid domain, denoted, by Γ_{wall}, no-slip boundary conditions were applied. The experimentally obtained flow-pulse given in Fig. 3 was approximated by a positive and a negative part of a sinus, and applied in the shape of a plug flow at the inlet (Γ_{in}) boundary. At the outlet (Γ_{out}) the tangential velocity and the normal component of the stress vector ($\boldsymbol{\sigma}_f \cdot \mathbf{n}_f$) were set to zero.

The stiff valve is considered to be an incompressible elastic solid strip. The momentum equation (4) and the incompressibility condition (5) of the solid are given by

$$\boldsymbol{\nabla} \cdot \boldsymbol{\sigma}_s = \mathbf{0} \quad \text{in} \qquad \Omega_s, \tag{4}$$

$$\det(\mathbf{F}) = 1 \quad \text{in} \qquad \Omega_s, \tag{5}$$

where $\boldsymbol{\sigma}_s$ is the Cauchy stress tensor of the solid, $\mathbf{F}$ the deformation tensor $\mathbf{F} = (\boldsymbol{\nabla}_0 \mathbf{x}_s)^{\mathrm{T}} = \mathbf{I} + (\boldsymbol{\nabla}_0 \mathbf{u}_s)^{\mathrm{T}}$, $\boldsymbol{\nabla}_0$ the gradient operator with respect to the initial configuration, $\mathbf{x}_s$ the solid position field and $\mathbf{u}_s$ the displacement vector. Body forces were neglected. The density of the rigid leaflet is assumed equal to the fluid density, allowing the buoyancy forces to be neglected. The inertia of the rigid valve is not taken into account since the mass of the leaflets is negligible with respect to the fluid mass.

The incompressible, isotropic material of the valve leaflet is subject to small strains. Therefore a physically linear constitutive model is used for the material behaviour. A geometrically nonlinear model is used to deal with the large rotations of the leaflet, describing the strain of the solid in an objective manner:

$$\boldsymbol{\sigma}_s = -p_s \mathbf{I} + \boldsymbol{\tau}_s, \quad \boldsymbol{\tau}_s = G(\mathbf{B} - \mathbf{I}) \quad \text{in} \qquad \Omega_s, \tag{6}$$

where p_s is the hydrostatic pressure in the solid and $\boldsymbol{\tau}_s$ the extra stress tensor. The extra stress tensor is a function of the shear modulus G and the left Cauchy-Green strain tensor $\mathbf{B}$ which is defined as $\mathbf{B} = \mathbf{F} \cdot \mathbf{F}^{\mathrm{T}}$.

The rigid leaflet is fixed at a point to the top right corner. At this point, the displacement is prescribed to be zero. As a result, free rotation of the leaflet around this point is allowed.

At the boundary of the solid domain Γ_s, which is completely immersed in Ω_f, the velocities of the fluid and the solid are coupled:

$$\mathbf{v}_f = \mathbf{v}_s = \dot{\mathbf{u}}_s \quad \text{on} \qquad \Gamma_s, \tag{7}$$

with $\dot{\mathbf{u}}_s$ the time derivative of the displacement field. Furthermore, the stress exerted by the solid on the fluid and the stress exerted on the solid by the fluid are in equilibrium at the boundary of the solid domain Γ_s:

$$\boldsymbol{\sigma}_f \cdot \mathbf{n}_f = \boldsymbol{\sigma}_s \cdot \mathbf{n}_s, \quad \text{on} \qquad \Gamma_s, \tag{8}$$

with $\mathbf{n}_s$ the outward normal of the solid domain and $\mathbf{n}_f$ the outward normal of the fluid domain, i.e. the opposite direction. However, the fluid domain does not have a physical boundary at the location of the boundary of the solid domain, which is where the fictitious domain method comes in.

In the original formulation of the fictitious domain method a variational approach is used. In this formulation, the use of Lagrange multipliers to establish coupling between fluid and structure is commonly applied. However, there exists no variational principle for the Navier–Stokes equations due to the nonlinear terms. Nevertheless, the method is used by deriving the weak form of the Stokes equation and adding the nonlinear term afterwards (Bertrand et al., 1997). Alternatively, the weighted residuals method can be applied. In this formulation, the stress exerted by the solid on the fluid can be regarded as a locally acting body force. Using the Dirac delta function, the body force $\mathbf{f}_f^*$ in Eq. (2) can be described as

$$\mathbf{f}_f^* = \mathbf{f}_f \delta(\mathbf{x} - \mathbf{x}_{\Gamma_s}) \quad \text{in} \qquad \Omega_f, \tag{9}$$

where $\mathbf{f}_f^*$ only has values not equal to zero at the fluid–structure interaction interface Γ_s. This introduces a globally acting surface force $\mathbf{f}_f$, localized at the interface Γ_s by means of the delta function. Making use of the property of the delta function, the body force term in the Navier–Stokes equation (2) can, in the weak form, be written as

$$\int_{\Omega_f} \mathbf{w}_f \cdot \mathbf{f}_f^* \, \mathrm{d}\Omega_f = \int_{\Omega_f} \mathbf{w}_f \cdot \mathbf{f}_f \delta(\mathbf{x} - \mathbf{x}_{\Gamma_s}) \, \mathrm{d}\Omega_f = \int_{\Gamma_s} \mathbf{w}_f \cdot \mathbf{f}_f \, \mathrm{d}\Gamma_s \quad \text{in} \qquad \Omega_f, \tag{10}$$

with $\mathbf{w}_f$ the weighting functions defined in the fluid domain. The rightmost expression in Eq. (10) is the same term as added to the system equations using the variational principle (Bertrand et al., 1997), where $\mathbf{f}_f$ is regarded as a Lagrange multiplier.

When deriving the weak formulation for the solid equations, partial integration results in a boundary integral in which the external load of the fluid on the valve can be incorporated:

$$\int_{\Omega_s} \mathbf{w}_s \cdot (\boldsymbol{\nabla} \cdot \boldsymbol{\sigma}_s)\, \mathrm{d}\Omega_s = -\int_{\Omega_s} (\boldsymbol{\nabla}\mathbf{w}_s)^{\mathrm{T}} : \boldsymbol{\sigma}_s\, \mathrm{d}\Omega_s + \int_{\Gamma_s} \mathbf{w}_s \cdot (\boldsymbol{\sigma}_s \cdot \mathbf{n}_s)\, \mathrm{d}\Gamma_s. \tag{11}$$

In order to reach an equilibrium of interaction forces, the last term in Eq. (11) must be in equilibrium with the right-hand-side of Eq. (10):

$$\int_{\Gamma_s} \mathbf{w}_s \cdot (\boldsymbol{\sigma}_s \cdot \mathbf{n}_s)\, \mathrm{d}\Gamma_s = \int_{\Gamma_s} \mathbf{w}_f \cdot \mathbf{f}_f\, \mathrm{d}\Gamma_s. \tag{12}$$

As the pressure p of Eq. (2) is used to weakly enforce the incompressibility constraint (Eq. (3)), the interaction force $\mathbf{f}_f$ is used as a Lagrange multiplier to weakly couple the velocities of the fluid and solid domain on nonconforming discretizations,

$$\int_{\Gamma_s} \mathbf{w}_i \cdot (\mathbf{v}_s - \mathbf{v}_f)\, \mathrm{d}\Gamma_s = 0, \tag{13}$$

with $\mathbf{w}_i$ the weighting functions defined on the fluid–structure interaction interface. Generally, the fluid–structure interaction interface entails the entire boundary Γ_s of the solid domain Ω_s. Extra coupling equations (Eq. (13)) are introduced where coupling is required. In the case of a thin leaflet, however, two sides of the boundary of the solid are very close to each other. This may lead to an overconstraining of velocity unknowns per element in the fluid domain. This may introduce deteriorating convergence properties of the solution procedure. To circumvent this problem, the interaction is approximated by only taking the upstream part (Γ_i) of the solid boundary Γ_s into account. As the valve leaflet is thin, this approximation will only influence transvalvular stresses and strains and it may be assumed not to influence the fluid–structure interaction.

In the momentum equation for the fluid, Eq. (2), as in the fluid–structure interaction equation (13), the velocity field is considered. However, the unknown quantity in the momentum equation for the solid is the displacement field $\mathbf{u}_s$. For the velocity field of the solid during a time-step a first-order approximation of the displacement field $\mathbf{u}_s$ is used:

$$\mathbf{v}_s = \frac{\mathbf{u}_s - \mathbf{u}_s^n}{\Delta t}, \tag{14}$$

where Δt represents the time-step. Summarizing, while writing $\boldsymbol{\sigma}_s \cdot \mathbf{n}_s = \mathbf{f}_s$, the weak form of the governing equations read:

$$\begin{aligned}\int_{\Omega_f} \rho\mathbf{w}_f \cdot \left(\frac{\delta\mathbf{v}_f}{\Delta t} + \hat{\mathbf{v}}_f \cdot \boldsymbol{\nabla}\delta\mathbf{v}_f + \delta\mathbf{v}_f \cdot \boldsymbol{\nabla}\hat{\mathbf{v}}_f\right) \mathrm{d}\Omega_f + \int_{\Omega_f} (\boldsymbol{\nabla}\mathbf{w}_f)^{\mathrm{T}} : \delta\boldsymbol{\tau}_f\, \mathrm{d}\Omega_f \quad - \int_{\Omega_f} (\boldsymbol{\nabla}\cdot\mathbf{w}_f)\delta p_f\, \mathrm{d}\Omega_f - \int_{\Gamma_i} \mathbf{w}_f \cdot \delta\mathbf{f}_f\, \mathrm{d}\Gamma_i = \\ - \int_{\Omega_f} \rho\mathbf{w}_f \cdot \left(\frac{\hat{\mathbf{v}}_f - \mathbf{v}^n}{\Delta t} + \hat{\mathbf{v}}_f \cdot \boldsymbol{\nabla}\hat{\mathbf{v}}_f\right) - (\boldsymbol{\nabla}\mathbf{w}_f)^{\mathrm{T}} : \hat{\boldsymbol{\sigma}}_f\, \mathrm{d}\Omega_f \quad + \int_{\Gamma_f} \mathbf{w}_f \cdot \mathbf{t}_f\, \mathrm{d}\Gamma_f + \int_{\Gamma_i} \mathbf{w}_f \cdot \hat{\mathbf{f}}_f\, \mathrm{d}\Gamma_i,\end{aligned} \tag{15}$$

$$\int_{\Omega_f} \mathbf{q}_f(\boldsymbol{\nabla}\cdot\delta\mathbf{v}_f)\, \mathrm{d}\Omega_f = -\int_{\Omega_f} \mathbf{q}_f(\boldsymbol{\nabla}\cdot\hat{\mathbf{v}}_f)\, \mathrm{d}\Omega_f, \tag{16}$$

$$\begin{aligned}\int_{\Omega_s} \Delta t(\boldsymbol{\nabla}\mathbf{w}_s)^{\mathrm{T}} : (\delta\boldsymbol{\tau}_s - (\boldsymbol{\nabla}\delta\mathbf{v}_s)^{\mathrm{T}} \cdot \hat{\boldsymbol{\sigma}}_s)\, \mathrm{d}\Omega_s - \int_{\Omega_s} \delta p\boldsymbol{\nabla}\cdot\mathbf{w}_s\, \mathrm{d}\Omega_s \\ - \int_{\Gamma_i} \mathbf{w}_s \cdot \delta\mathbf{f}_s\, \mathrm{d}\Gamma_i = -\int_{\Omega_s} (\boldsymbol{\nabla}\mathbf{w}_s) : \hat{\boldsymbol{\sigma}}_s\, \mathrm{d}\Omega_s + \int_{\Gamma_i} \mathbf{w}_s \cdot \hat{\mathbf{f}}_s\, \mathrm{d}\Gamma_i,\end{aligned} \tag{17}$$

$$\int_{\Omega_s} q_s \Delta t(\boldsymbol{\nabla}\cdot\delta\mathbf{v}_s)\, \mathrm{d}\Omega_s = -\int_{\Omega_s} q_s \frac{(\hat{J}-1)}{\hat{J}}\, \mathrm{d}\Omega_s, \tag{18}$$

$$\int_{\Gamma_s} \mathbf{w}_i \cdot (\delta\mathbf{v}_f - \delta\mathbf{v}_s)\, \mathrm{d}\Gamma_s = -\int_{\Gamma_i} \mathbf{w}_i \cdot (\hat{\mathbf{v}}_f - \hat{\mathbf{v}}_s)\, \mathrm{d}\Gamma_i. \tag{19}$$

Temporal discretization of the Navier–Stokes equation (15) is achieved using an implicit Euler scheme, while the linearization of the convective term $\mathbf{v}_f \cdot \boldsymbol{\nabla}\mathbf{v}_f$ is obtained using Newton's method including iterations during a time-step.

The two-dimensional representation of the aortic root shown in Fig. 5 was discretized to a finite element mesh. Fig. 6 shows the part of the mesh near the sinus cavity. The length of the inlet channel is $4H$ while the length of the outlet channel is 10 times the height of the channel.

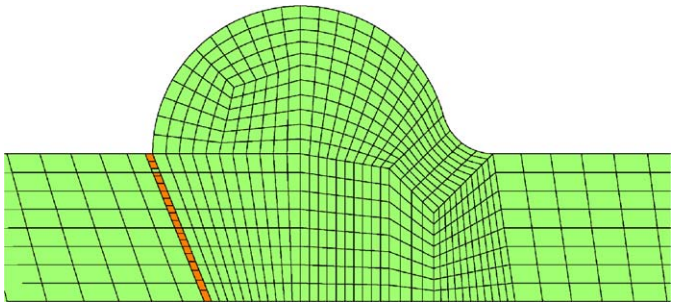

Fig. 6. Section near the sinus cavity of the mesh used for the finite element computations. The valve leaflet, located in the transition from the inflow channel (left) to the sinus cavity, is shown in closed configuration and is represented by the darker elements.

In this figure the rigid leaflet is shown in closed position. The length of the leaflet is $1.07H$, so the leaflet in closed position is under an angle of approximately 22° with the vertical. The thickness of the leaflet is 1 mm.

Galerkin's method is used for the spatial discretization, using 834 rectangular quadratic Crouzeix–Raviart elements. For the structure, spatial discretization is obtained using 19 rectangular quadratic Crouzeix–Raviart elements. The discretization of the Lagrange multiplier in Eq. (19) is chosen discrete and coincides with the mid-points of the upstream edges of the solid elements of the leaflet. Gaussian integration was used to compute the integrals of the weak forms of the governing equations. The resulting system to be solved is given by

$$\begin{pmatrix} \begin{bmatrix} \underline{K}_f^* & \underline{L}_f^{\mathrm{T}} \\ \underline{L}_f & \underline{0} \end{bmatrix} & [\underline{0}] & \begin{bmatrix} \underline{C}_f^{\mathrm{T}} \\ \underline{0} \end{bmatrix} \\ [\underline{0}] & \begin{bmatrix} \underline{K}_s^* & \underline{L}_s^{\mathrm{T}} \\ \underline{L}_s^* & \underline{0} \end{bmatrix} & \begin{bmatrix} \underline{C}_s^{\mathrm{T}} \\ \underline{0} \end{bmatrix} \\ [\underline{C}_f \;\; 0] & [\underline{C}_s \;\; 0] & [\underline{0}] \end{pmatrix} \cdot \begin{pmatrix} \delta \underset{\sim}{v}_f \\ \delta \underline{p}_f \\ \delta \underset{\sim}{v}_s \\ \delta \underline{p}_s \\ \delta \underset{\sim}{f}_c \end{pmatrix} = \begin{pmatrix} \underset{\sim}{f}_f^v \\ \underline{f}_f^p \\ \underset{\sim}{f}_s^v \\ \underline{f}_s^p \\ \underset{\sim}{f}_c \end{pmatrix}, \tag{20}$$

where $\underline{K}_f^*$ is the fluid matrix, $\underline{K}_s^*$ the solid matrix, $\underline{L}_f$ and $\underline{L}_s$ the divergence matrices for the fluid and solid phase, $\underline{C}_f$ and $\underline{C}_s$ the fluid and solid matrices concerning the coupling of the fluid and solid velocity. The variations in the estimates for the fluid velocity, solid velocity, fluid pressure, solid pressure and coupling force are represented by $\delta \underset{\sim}{v}_f, \delta \underset{\sim}{v}_s, \delta \underline{p}_f, \delta \underline{p}_s$, and $\delta \underset{\sim}{f}_c$, respectively. For more details on this subject and the definitions of the submatrices, the reader is referred to Appendix A of de Hart (2002), or van de Vosse et al. (2003). The linearized system is solved in a fully coupled manner using a direct solver.

3. Results

3.1. Fluid motion

Fluid velocity vector fields were measured in an in vitro set-up of the aortic root with a rigid valve in the sinus cavity, and simulated using the computational model, as described in the previous section.

Fig. 7 shows the velocity fields as obtained by the PIV-measurements at five instants in time in the flowcycle, as indicated in panel (f), for a Reynolds number of 750 and a Strouhal number of 0.055. Panel (a) shows the velocity field for peak flow rate. Closer examination reveals that the fluid velocity in the entire channel can be described as a plug flow in the centre with a boundary layer near the top and the bottom walls of the channel (see also Fig. 9). In the sinus cavity a very weak vortex is present downstream the tip of the valve leaflet. In panel (b), the deceleration of the fluid has initiated the development of a large vortex in the sinus cavity. Further along in the flow-pulse, the flow changes direction and backflow occurs. This reversed flow is necessary for the valve to reach its closed position. In panel (c) the reversed flow has reached its maximum value. The large vortex in the sinus cavity has grown and now fills the entire cavity. Downstream of the large vortex, a second vortex has developed which is much smaller and rotates in the opposite direction. The fluid motion at the end of the backflow period is shown in panel (d). The two vortices are still present and the secondary vortex has increased slightly in size.

Because of the settings of the flow-pulse, the valve has now just reached its closed position. The fluid now accelerates further to the mean value of the cyclic flow rate, for which the velocity field is shown in panel (e). The velocity in the in-

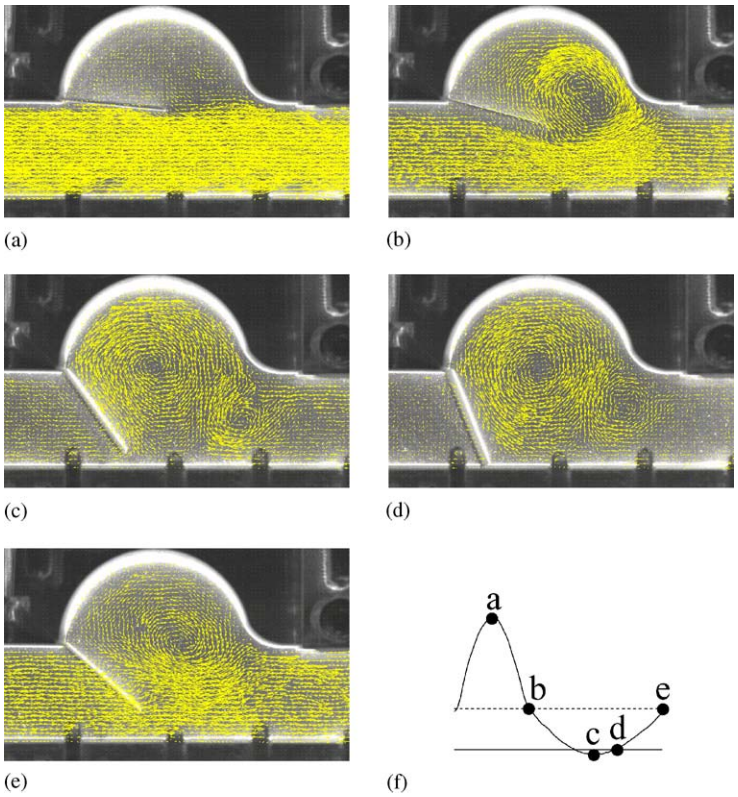

Fig. 7. Measured velocity vector fields superimposed on the images captured by the PIV-camera for five instants of time in the flow-cycle: (a) peak flow rate, (b) average flow rate in deceleration, (c) peak reversed flow rate, (d) end of backflow and (e) average flow rate in acceleration. These instants are illustrated in the flow-pulse (f); Re = 750 and Sr = 0.055.

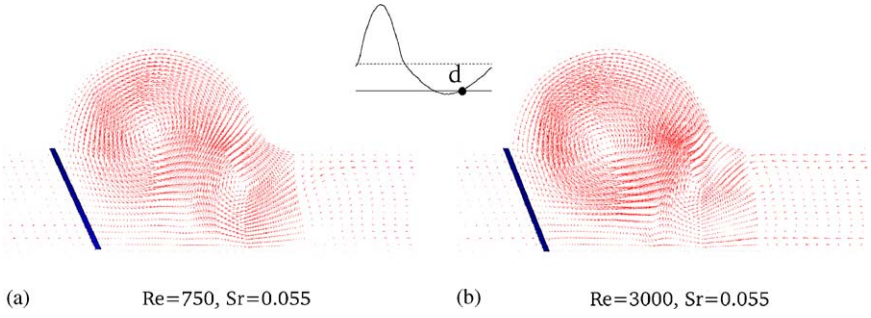

Fig. 8. Computational result at the end of backflow (indicated as instant of time *d* in the flow curve), showing the velocity field at the moment that the valve is almost completely closed. The Strouhal number in these simulations is 0.055 with Reynolds numbers of (a) 750 and (b) 3000.

and outflow channel is increased and the large vortex in the cavity is being suppressed. The secondary vortex has already diminished.

Fig. 8 shows the computational results at the end of backflow (indicated as instant of time *d* in the flow curve, see also Fig. 7(f)), at the moment when the valve is almost completely closed. Panel (a) shows the results of the simulation with Reynolds and Strouhal numbers being 750 and 0.055, respectively. In agreement with the experiments (Fig. 7(d)), a large vortex has formed in the sinus cavity, downstream of which a smaller counter-rotating vortex has formed. Panel (b) shows the result at the same instant in the flow-pulse as in panel (a), but now for a Reynolds number of 3000. Note that the main flow characteristics are similar, though the strength of the large vortex is increased, the secondary vortex

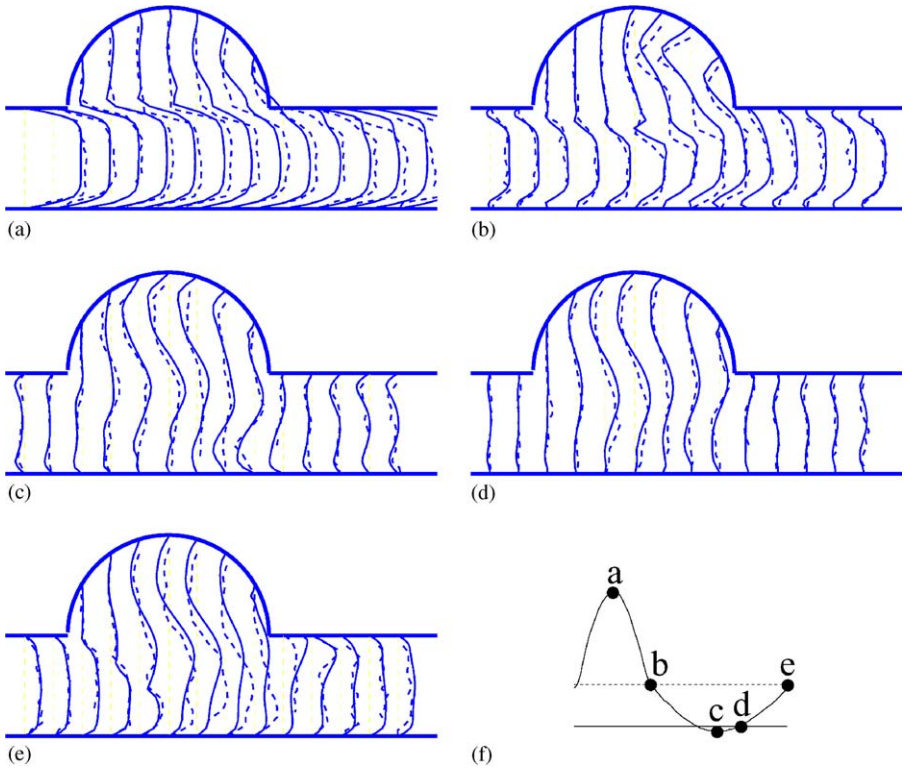

Fig. 9. Interpolated horizontal velocity components at several cross-sections of the channel at five points in the flow cycle; (a) peak flow, (b) average flow rate in deceleration, (c) maximum reversed flow rate, (d) end of reversed flow, and (e) mean flow rate during acceleration. The computations are represented by the solid lines, the experiments by the dashed lines; Re = 750 and Sr = 0.055.

is located slightly further upstream and the unsteady boundary layer flow near the top and bottom of the outflow channel is more pronounced.

Quantitative comparison of the experimental and computational velocity fields is given in Fig. 9. Hereto, the horizontal components of both flow fields were interpolated to several cross-sections in the channel. The interpolations shown in Fig. 9 are given for the same five instants in the flowcycle as in Fig. 7.

Generally, the computed velocity field matches the experiments quite well. However, apart from local differences as a result of measurement and computational inaccuracies, there are some striking global differences. During the entire cycle, the computed vortex in the cavity is more pronounced and is located slightly higher than the experimentally observed vortex. During the deceleration of the fluid (b) and just beyond (c), in the boundary layers near the top and bottom walls of the channel, reversed flow occurs due to the unsteady nature of the flow. This kind of Womersley profiles are not detected well by the PIV measurements. Furthermore, during acceleration (subfigure e) the measured velocity below and downstream the tip of the valve is higher than predicted by the computational method.

3.2. Valve motion

The motion of the valve is expressed in terms of the time-course of the opening angle of the valve, defined as the angle between the valve leaflet and the vertical (see Fig. 5). Fig. 10 shows a graph of the normalized average in-flow velocity and opening angle of the valve for the entire flowcycle, measured from the camera images.

The flow-pulse is normalized with the maximum flow rate (Q/Q_{max}) and divided by the cross-sectional area to obtain the normalized average inflow velocity (V/V_{max}), while the opening angle of the valve is normalized by dividing the difference between the opening angle of the valve and the closed angle by the range of the opening angle: $(\alpha-\alpha_{min})/(\alpha_{max}-\alpha_{min})$.

The curves in Fig. 10 show that during acceleration of the fluid, the opening angle of the valve increases. The valve reaches its maximum opening angle just after peak flow rate. During early deceleration, the valve opening angle starts to

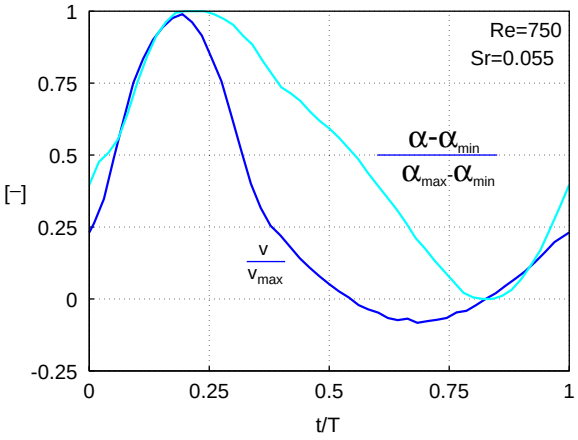

Fig. 10. Experiment: normalized measured fluid velocity (v/v_{max}) and normalized valve opening angle ($(\alpha-\alpha_{min})/(\alpha_{max}-\alpha_{min})$) as a function of the cycle time (t/T).

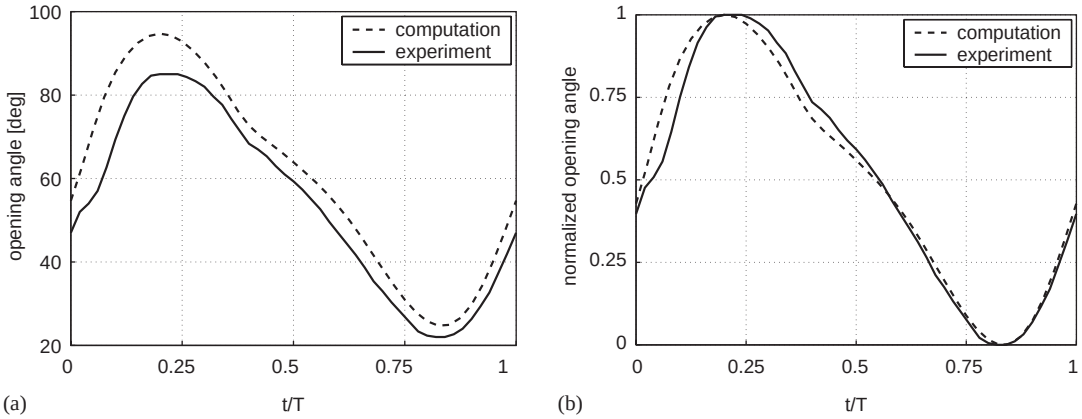

Fig. 11. (a) Valve opening angles observed in the experiments (solid line) and computational prediction (dashed line); (b) normalized curves.

decrease, while the flow upstream the valve is still directing forward. The closing motion of the valve is approximately linear in time. In order to close the valve, a small amount of backflow (regurgitation) was necessary. At the end of the backflow the valve is closed, which is shown in Fig. 10 where the curves of the fluid inflow velocity and the normalized opening angle cross the zero line and each other.

Fig. 11(a) shows the experimentally observed and computationally predicted opening angle of the valve. The computed angles exceed the measured ones during the entire cycle. This is most pronounced near the maximum opening angle and least near the closed position. Note that the valve is closed at an angle of 22°. The timing of the computed valve motion closely matches the experimentally observed pattern, which is better visible in Fig. 11(b) where both curves are normalized. Furthermore, the experimentally observed opening angle slightly lags behind the computationally predicted values for high fluid accelerations.

3.3. Dependence of valve motion on flow conditions

In order to study to what extent the valve motion is influenced by the characteristics of the flow-pulse, the experiment was performed under several flow conditions as presented in Table 1. Fig. 12(a) shows the average velocity over the inflow area during a cycle for each flow case. The difference in time period is clear, as is the lower maximum flow rate for a Reynolds number equal to 500. For each flow case, a different amount of backflow was necessary to close the

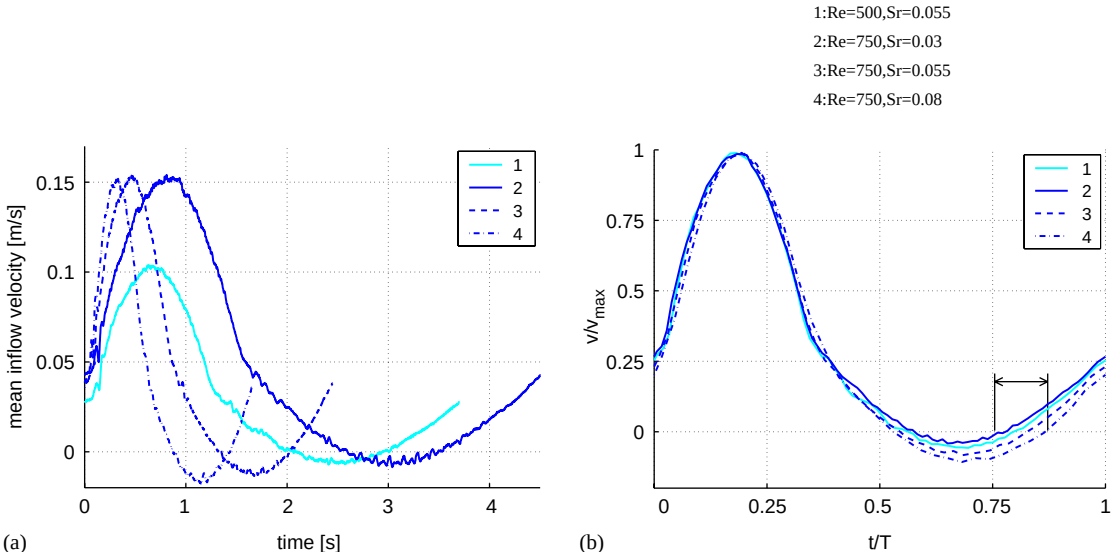

Fig. 12. (a) Average in-flow velocity derived from measurements of the applied flow-pulses versus time for each flow case; (b) normalized velocity versus normalized time. The curves in panel (b) show that the maximum reversed flow-rate and the end of backflow were different for each flow case.

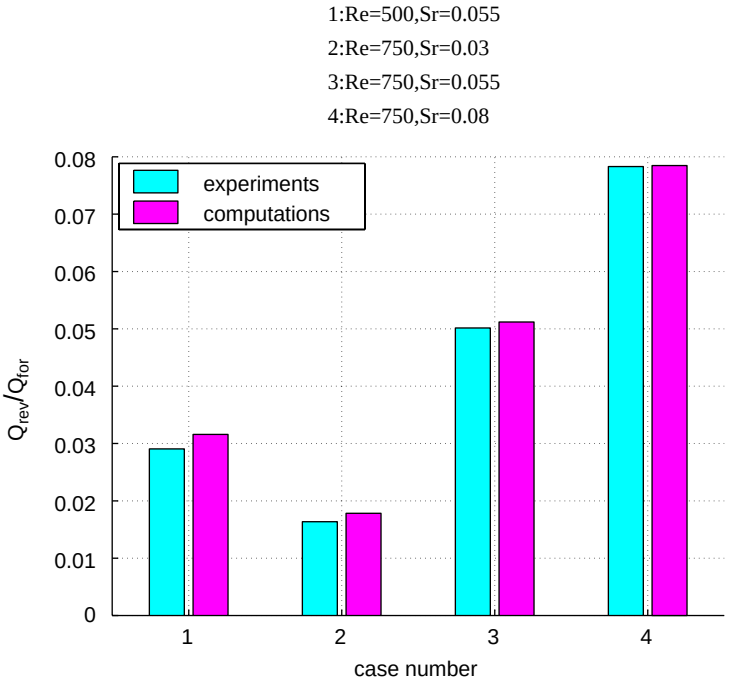

Fig. 13. Backflow divided by forward flow of measured flow curves (light bars) and flow-pulses applied to the computational model (dark bars).

valve. Fig. 12(b) shows the same data, normalized by the time period and peak velocity. Since the valve is closed when the velocity curve rises through zero, this figure shows that the moment of valve closure was different for each case (see arrow in Fig. 12(b)).

Fig. 13 shows the relative amount of backflow with respect to the amount of forward flow $Q_{\text{reversed}}/Q_{\text{forward}}$ for each flow condition, both for the experiments and the computations. It is shown that for increasing the Reynolds number from 500 to 750 (by increasing the velocity), while keeping the Strouhal number at 0.08 (by keeping TV constant), the amount of backflow increases with respect to the amount of forward flow. The same occurs when the Strouhal number is increased (by decreasing the time period), while keeping the Reynolds number at 750. Due to the noise on the flow measurement, the relative amount of backflow is not exactly the same as applied to the computational model.

Fig. 14 shows that, for every flow condition, the valve reaches its closed position at the end of the backflow phase. Furthermore it shows that, for increasing either the Strouhal number (decreasing T) or the Reynolds number (increasing V and keeping TV constant), the valve reaches its closed position later in the flow-cycle, as predetermined by the flow-pulse applied, and also that the valve reaches its maximum opening angle later for increasing either the Reynolds or the Strouhal number within the range applied.

The instant of time of valve closure in the flow cycle is clarified in the bar plot of Fig. 15(a). In this figure the left bar of each set shows the experimentally obtained moment at which the valve is closed, measured from the start of the flow-pulse as shown in Fig. 12(b) for each case. The range ($n=3$) of the time of valve closure is given by the errorbars. In the same way, panel (b) of Fig. 15 shows the duration of valve opening, from closed to opened position. The experimentally observed duration of valve opening increases for increasing Strouhal number or decreasing Reynolds number, although not significantly.

The bars on the right of Fig. 15(a) and (b) show the predictions for the time of minimum opening angle and the duration of the opening motion of the valve with the computational model. The prediction of the moment in the flow-pulse at which the opening angle is minimal matches the experimentally observed values. The difference between the two is maximal for case 4, but still lies within the range of experimental data. In the computational model, the same trend is found for the duration of the opening motion of the valve. The maximum difference in opening is seen in case 1 (the low Reynolds number case), which also lies within the range of the experimental data.

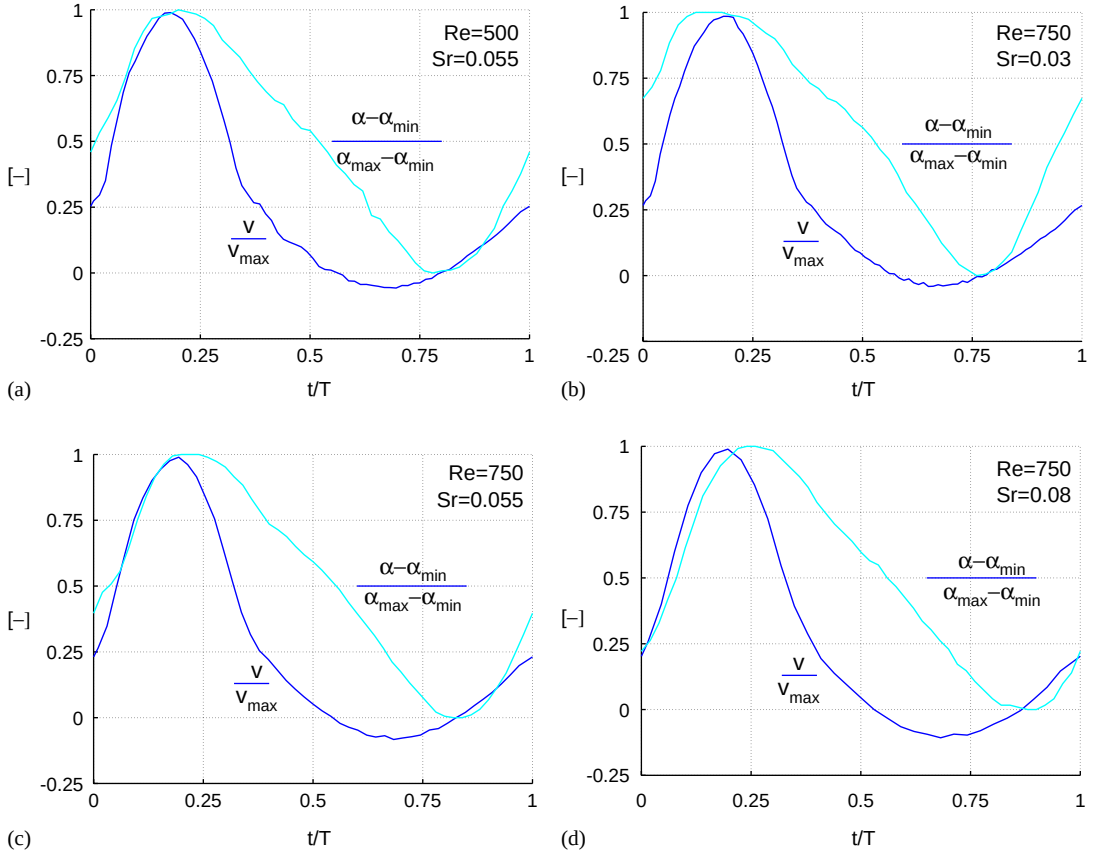

Fig. 14. Measured normalized in-flow velocity and normalized opening angle for each flow case.

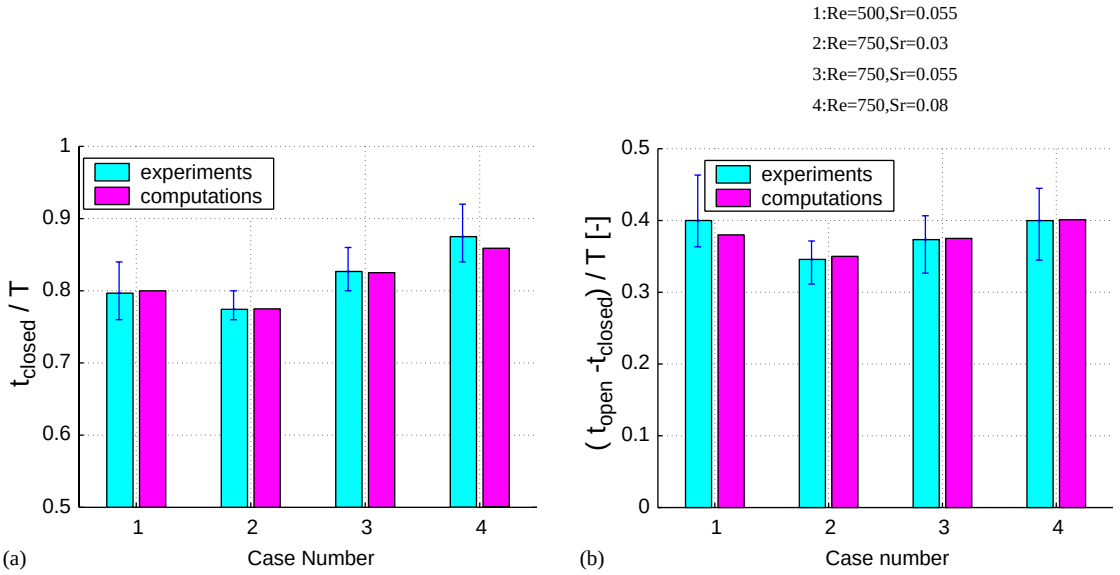

Fig. 15. (a) Time of smallest valve opening angle and (b) duration of opening motion of the valve for each case. Experimental data in light bars with errorbar giving data range ($n=3$), computational data in dark bars.

4. Discussion

In an experimental set-up of the aortic valve, fluid and valve motion were recorded by the camera of a PIV system. Instantaneous fluid velocity fields were derived by correlating average particle displacement within interrogation areas of subsequent camera images, under the assumption of small velocity gradients in the interrogation area. This condition is fulfilled in the major part of the measurement section. However, the unsteady boundary layers developing near the top and bottom walls of the in- and outflow channel during deceleration are not well detected by the PIV method, since these velocity structures are too small for the interrogation areas. This can be solved by increasing the resolution of the camera, or decreasing the field of view combined with the use of smaller seeding particles.

A two-dimensional finite element model of the experiment is developed, in which fluid–structure interaction is modelled by means of a fictitious domain method, as described in Glowinski et al. (1994) and Bertrand et al. (1997), but formulated in terms of a locally acting volume force. The system matrix, arising after discretization of the governing equations of the solid and the fluid, is ill-conditioned. The eigenvalues of the matrix are related to the stiffness of the solid and the viscosity of the fluid, which differ by several orders of magnitude. Nonetheless, no stability problems occurred in solving the set of equations.

The experimental results showed the development of a large vortex in the sinus cavity during fluid deceleration. Further downstream a secondary counter-rotating vortex develops. During acceleration, these vortices diminish. These phenomena are also found using a flexible valve leaflet, as reported in de Hart et al. (2000). The valve opens due to the forward flow-pulse in the in-flow channel during acceleration. In agreement with previous observations (van Steenhoven and van Dongen, 1979) the vortex in the sinus cavity initiates valve closure in early deceleration, even though the in-flow velocity is still directed forward. A certain amount of regurgitation is necessary to close the valve completely. The computational results correctly predict the main characteristics of fluid and valve motion. The computed timing of valve motion, in terms of minimum opening angle and duration of valve opening, lies within the experimental range. However, the computationally predicted valve opening angle exceeds the angle observed in the experiments. This mismatch increases during fluid acceleration. A possible explanation for this effect is that in the experiments the valve motion is hampered by the boundary layer flow near the sidewalls of the set-up. This effect is not present in the two-dimensional computational model. Furthermore, since the valve is fixed to the top of the in-flow channel using three strips of adhesive tape, a small amount of fluid can leak over the top of the valve between the strips of tape. When the valve is closed and the fluid starts to move forward, the fluid passing underneath the valve will push the valve open. Since some of the fluid will leak over the valve, the valve will possibly not open as far as without the leakage.

In the entire region, the measured and computed flow patterns match very well. The slight differences are probably caused by the difference in valve motion. As the valve opening angle is larger in the computations, the large vortex in

the sinus cavity will be more near the top of the cavity. During acceleration in the experiments, the fluid has to squeeze through a smaller opening due to the smaller opening angle of the valve. Since the same amount of fluid is entering the cavity, the fluid velocity underneath the valve tip is higher than in the computational results.

Another possible source for the discrepancy between computational and experimental results can be sought in the fact that fluid–structure interaction was taken into account at the upstream side of the valve only. It was assumed that this approximation is allowed, as the valve is thin compared to the flow structures. Moreover, during most of the acceleration and deceleration, the direction of flow is perpendicular to the valve surface, which is not likely to cause a deviation in the opening angle of the valve. Refining the fluid mesh to element sizes smaller than the thickness of the valve leaflet will enable the coupling of fluid and valve velocity at both the up- and downstream side of the valve. In this way, the error made by coupling at the upstream side only could be determined. It will, however, require a substantial increase in CPU-time.

Four cases with different inflow characteristics were applied to both the experimental and the computational model. Experiments showed that the duration and maximum value of backflow, necessary to close the valve, was different for each case. This means, since the shape of the pulse is fixed, that valve closure occurs at different instants in time in the flow-cycle. The development of vortices in the cavity during deceleration is influenced by changing the Strouhal or Reynolds number of the in-flow. The valve leaflet interacts with these vortices and therefore the valve motion is influenced by the characteristics of the in-flow condition. The experimental results showed that there is a weak trend of increasing duration of valve opening for increasing Strouhal number or decreasing Reynolds number. The same trend is observed in the computational results. However, taking into account the range in experimental data, this trend is not statistically significant.

In the model by Horsten (1990) the valve motion was modelled using an ALE-method. The method does not allow the valve to fully close, since the fluid elements between the wall and the leaflet will be compressed. This is not a problem for the fictitious domain method, nor for the Immersed Boundary method by Peskin and McQueen (1995). The method by Peskin and McQueen (1995) was not applied for physiological Reynolds numbers due to numerical stability problems. In order to obtain numerical stability the viscosity was increased by a factor 25, resulting in a Reynolds number of 80. With the computational model presented in this work, no stability problems occurred for simulations with Reynolds numbers up to the physiologically relevant value of 3000. However, the experimental set-up did not allow validation of the simulations with Reynolds and Strouhal numbers within this physiological range. In order to apply the present method to a valve in the heart, the closed valve will have to be able to carry the pressure difference between the ventricle and the aorta or the atrium. This situation could not be simulated with the experimental set-up and will need further investigation.

Computations in three-dimensional geometries will enable studies to more realistic situations. For flexible valves, extension of the method to three dimensions is straightforward, as shown by de Hart et al. (2003).

From the results, it may be concluded that the fictitious domain method was successfully applied for modelling rigid heart valve motion. In the range of flow-pulses applied to the experimental and the computational model, the sensitivity of the time-dependent response of the valve to changes in the applied flow-pulse was low (maximum deviation in duration of opening about 5% of the period time (see Fig. 15)), but still well predicted by the computational method.

References

Baaijens, F.P.T., 2001. A fictitious domain/mortar element method for fluid–structure interaction. International Journal for Numerical Methods in Fluids 35, 743–761.

Baccani, B., Domenichini, F., Pedrizzetti, G., 2003. Model and influence of mitral valve opening during the left ventricular filling. Journal of Biomechanics 36, 355–361.

Bertrand, F., Tanguy, P.A., Thibault, F., 1997. A three-dimensional fictitious domain method for incompressible fluid flow problems. International Journal for Numerical Methods in Fluids 25, 719–736.

Bluestein, D., Rambod, E., Gharib, M., 2000. Vortex shedding as a mechanism for free emboli formation in mechanical heart valves. ASME Journal of Biomechanical Engineering 122, 125–134.

Bluestein, D., Li, Y.M., Krukenkamp, I.B., 2002. Free emboli formation in the wake of bi-leaflet mechanical heart valves and the effects of implantation techniques. Journal of Biomechanics 35, 1533–1540.

Cape, E.G., Sung, H., Yoganathan, A.P., 1996. Hemodynamica assessment of carbomedics bileaflet heart valves by ultrasound: studies in the aortic and mitral positions. Ultrasound in Medicine & Biology 22, 421–430.

Chandran, K.B., Shoephoerster, R., Dellsperger, K.C., 1989. Effect of prosthetic mitral valve geometry and orientation on flow dynamics in a model human left ventricle. Journal of Biomechanics 22, 51–65.

de Hart, J., 2002. Fluid–stucture interaction in the aortic heart valve. Ph.D. Thesis, Eindhoven University of Technology, The Netherlands.

de Hart, J., Peters, G.W.M., Schreurs, P.J.G., Baaijens, F.P.T., 2000. A two-dimensional fluid-structure interaction model of the aortic valve. Journal of Biomechanics 33, 1079–1088.

de Hart, J., Peters, G.W.M., Schreurs, P.J.G., Baaijens, F.P.T., 2003. A three-dimensional computational analysis of fluid–structure interaction in the aortic valve. Journal of Biomechanics 36, 103–112.

Fatemi, R., Chandran, K.B., 1989. An in vitro comparative study of St. Jude Medical and Edwards–Duromedics bileaflet valves using laser anemometry. ASME Journal of Biomechanical Engineering 111, 298–302.

Garitey, V., Gandelheid, T., Fusezi, J., Pelissier, R., Rieu, R., 1995. Ventricular flow dynamic past bileaflet prosthetic heart valves. International Journal of Artificial Organs 18, 380–391.

Glowinski, R., Pan, T.W., Periaux, J., 1994. A fictitious domain method for Dirichlet problem and applications. Computer Methods in Applied Mechanics and Engineering 111, 283–303.

Grigioni, M., Daniele, C., D'Avenio, G., Barbaro, V., 2001. The influence of the leaflets' curvature on the flow field in two bileaflet prosthetic heart valves. Journal of Biomechanics 34, 613–621.

Horsten, J.B.A.M., 1990. On the analysis of moving heart valves: a numerical fluid–structure interaction model. Ph.D. Thesis, Eindhoven University of Technology, The Netherlands.

Kilner, P.J., Yang, G.Z., Wilkes, A.J., Mohiaddin, R.H., Firmin, D.N., Yacoub, M.H., 2000. Asymmetric redirection of flow through the heart. Nature 404, 759–761.

King, M.J., Corden, J., David, T., Fisher, J., 1996. A three-dimensional, time-dependent analysis of flow through a bileaflet mechanical heart valve: comparison of experimental and numerical results. Journal of Biomechanics 29 (5), 609–618.

Krafczyk, M., Cerrolaza, M., Schulz, M., Rank, E., 1998. Analysis of 3d transient blood flow passing through an artificial aortic valve by lattice-Boltzmann methods. Journal of Biomechanics 31, 453–462.

Kwak, D.Y., Im, Y.T., 2003. Hexahedral mesh generation for remeshing in three-dimensional metal forming analyses. Journal of Materials Processing Technology 6691, 1–7.

Lemmon, J.D., Yoganathan, A.P., 2000. Three-dimensional computational model of left heart diastolic function with fluid–structure interaction. ASME Journal of Biomechanical Engineering 122, 109–117.

Lim, W.L., Chew, Y.T., Chew, T.C., Low, H.T., 2001. Pulsatile flow studies of a procine bioprosthetic aortic valve in vitro: PIV measurements and shear-induced blood damage. Journal of Biomechanics 34, 1417–1427.

Patankar, S.V., 1983. Numerical Heat Transfer and Fluid Flow. Hemisphere Publishing Corporation, McGraw-Hill, New York.

Peskin, C.S., 1972. Flow patterns around heart valves: a numerical method. Journal of Computational Physics 10, 252–271.

Peskin, C.S., McQueen, D.M., 1995. A general method for the computer simulation of biological systems interacting with fluid. Society for Experimental Biology 49, 265–276.

Pop, G., Sutherland, G.R., Roelandt, J., Vletter, W., Bos, E., 1989. What is the ideal orientation of a mitral disc prosthesis? An in vivo haemodynamic study based on colour flow imaging and continuous wave doppler. European Heart Journal 10, 346–353.

Reul, H., Talukder, N., Muller, E.W., 1981. Fluid mechanics of the natural mitral valve. Journal of Biomechanics 14 (5), 361–372.

van de Vosse, F.N., van Oijen, C.H.G.A., Bessems, D., Gunther, T.W.M., Wolters, B.J.B.M., Stijnen, J.M.A., de Hart, J., Baaijens, F.P.T., 2003. Fluid–structure interaction models in cardiovascular biomechanics. Journal of Engineering Mathematics 47, 335–368.

van Steenhoven, A.A., van Dongen, M.E.H., 1979. Model studies of the closing behaviour of the aortic valve. Journal of Fluid Mechanics 90 (1), 21–32.

Vierendeels, J.A., Riemslagh, K., Dick, E., Verdonck, P.R., 2000. Computer simulation of intraventricular flow and pressure gradients during diastole. ASME Journal of Biomechanical Engineering 122, 667–674.

Vlachos, P.P., Pierrakkos, O., Phillips, A., Telionis, D.P., 2001. Vorticity and turbulence characteristics inside a transparent flexible left ventricle. Proceedings of the 2001 ASME Bioengineering Conference, BED-Vol. 50, pp. 493–495.

Walker, P.G., Cranney, G.B., Grimes, R.Y., Delatore, J., Rectenwald, J., Phost, G.M., Yoganathan, A.P., 1996. Three-dimensional reconstruction of the flow in a human left heart by using magnetic resonance phase velocity encoding. Journal of Biomedical Engineering 24, 139–147.

Westerweel, J., 1993. Digital particle image velocimetry, theory and application. Ph.D. Thesis, Delft University of Technology, The Netherlands.

Willert, C.E., Gharib, M., 1991. Digital particle image velocimetry. Experiments in Fluids 10, 181–193.